SCIENTIFIC REPORTS

natureresearch

Check for updates

OPEN

Effects of conical intersections on hyperfine quenching of hydroxyl OH in collision with an ultracold Sr atom

Ming Li[1], Jacek Kłos[1,2], Alexander Petrov[1,3,4], Hui Li[1] & Svetlana Kotochigova[1✉]

The effect of conical intersections (CIs) on electronic relaxation, transitions from excited states to ground states, is well studied, but their influence on hyperfine quenching in a reactant molecule is not known. Here, we report on ultracold collision dynamics of the hydroxyl free-radical OH with Sr atoms leading to quenching of OH hyperfine states. Our quantum-mechanical calculations of this process reveal that quenching is efficient due to anomalous molecular dynamics in the vicinity of the conical intersection at collinear geometry. We observe wide scattering resonance features in both elastic and inelastic rate coefficients at collision energies below $k_B \times 10$ mK. They are identified as either p- or d-wave shape resonances. We also describe the electronic potentials relevant for these non-reactive collisions, their diabatization procedure, as well as the non-adiabatic coupling between the diabatic potentials near the CIs.

A diverse list of promising applications for ultracold molecular processes governed by quantum mechanics exists. This includes creating new types of sensors[1], advancing quantum information science[2–4], simulation of complex exotic materials[5,6], performing precision spectroscopy to test the Standard Model of particle physics[7–10], and, excitingly, the promise of quantum control of chemical reactions[11–13] as each molecule can be prepared in a unique ro-vibrational quantum state. In all these applications the ability to control the internal and external degrees of freedom of the cold molecular species is essential. At high temperatures, the state population distribution in molecular gasses is often spread over many quantum states, obscuring the key role of quantum effects. Therefore, over the past three decades much attention of the scientific community has been directed to developing techniques to cool molecules to cold (< 1 K) and ultracold (< 1 mK) temperatures as well as study their collective properties in the ultracold domain.

The coldest di-atomic molecules are now produced by magneto- and photo-association from laser-cooled alkali-metal atoms[6]. In fact, the associated dimers are prepared in their lowest ro-vibrational level and have translational temperatures below 1 μK. Despite this success, the association method only provides access to a limited range of molecular species. There exist many molecules, both di-atomic and polyatomic, that can not be easily formed from ultracold atoms. One such molecule is the hydroxyl radical OH as oxygen atoms has not been yet laser cooled. This molecule has attracted attention due to promising applications in precision measurement and quantum computation[14–17]. In addition, OH is an important molecule in understanding the behavior of interstellar media, astrophysical research[18–20], and atmospheric and climate science[21].

Evaporative cooling of hydroxyl, OH molecules loaded from Stark decelerators has so far been the method of choice to create molecular gasses with a few mK temperature[22]. Further cooling of these molecules to temperatures below 1 mK is desirable. One of the promising direct cooling techniques, proposed in Refs.[23,24], is the sympathetic cooling of molecules in thermal contact with laser-cooled neutral atoms. There have been numerous proposals to achieve sympathetic cooling using different atom-molecule pairs. See, for example, Refs.[25,26]. However, for various combinations of atoms and molecules inelastic collisions are projected to occur more

[1]Department of Physics, Temple University, Philadelphia, PA 19122, USA. [2]Department of Physics, Joint Quantum Institute, University of Maryland, College Park, MD 20742, USA. [3]NRC, Kurchatov Institute PNPI, Gatchina, Russia 188300. [4]Division of Quantum Mechanics, Saint Petersburg State University, St. Petersburg, Russia 199034. ✉email: skotoch@temple.edu
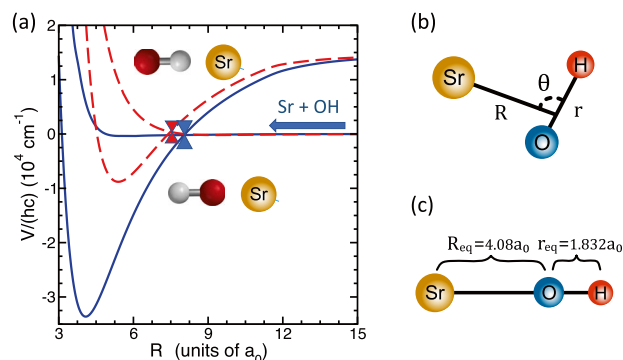
Figure 1. Relevant two-dimensional potential energy surfaces of non-reactive Sr + OH($^2\Pi$) as functions of Jacobi coordinates R. (**a**) Potential energies of the $1\,^2A'(X^2\Sigma^+)$ and $4\,^2A'(F^2\Pi)$ states as functions of R at $\theta = 180°$ (blue solid curves) and $\theta = 0°$ (dashed-red curves), respectively. Red and blue cones indicate conical intersections between X and F curves. They are located at $R = 7.4a_0$ and $8.1a_0$, respectively. The arrow marks the entrance channel. (**b**) A schematic depiction of the Jacobi coordinates. (**c**) Jacobi coordinates of the SrOH molecule in optimized geometry.

frequently than elastic collisions leading to overwhelming trap losses. A favorable elastic-to-inelastic ratio has been predicted for collisions of OH with atomic hydrogen with initial OH temperatures around 250 mK[27].

Sympathetic cooling of the internal states of neutral molecules with laser-cooled neutral atoms is far more challenging. Trap depths for neutral molecules are small and the energy release from vibrational, rotational, and even hyperfine relaxation rapidly decreases the number of cold molecules. On the other hand molecular ions, trapped in deep Penning or Paul traps, can survive sympathetic cooling of the internal states. The method was first demonstrated for the BaCl$^+$ molecular ion colliding with ultracold calcium[28] and further analyzed in Ref.[29]. A collision of this molecular ion with a polarizable ultracold atom encourages the two to thermalize via vibrational relaxation and elastic momentum-changing collisions.

Here, we examine the possibility of sympathetic cooling of external and internal degrees of freedom of OH molecules in their electronic $X^2\Pi_{3/2}$ ground state due to collisions with ultracold ground-state Sr atoms. We have developed a state-of-the-art quantum coupled-channel description of the OH + Sr system, thereby, allowing the calculations of collisional (elastic) and quenching (inelastic) rate coefficients. Our earlier study of the collisional complex SrOH[30] has proven that symmetry-required conical intersections (CIs) exist between its ground and excited $^2A'$ adiabatic electronic potential energy surfaces (PESs). Conical intersections are sets of degeneracy points between adiabatic PESs and are common features in the electronic structure of polyatomic molecules[31,32]. They play an important role in ultrafast radiation-less transitions from excited to ground electronic states found in photochemistry, molecular spectroscopy, and quantum reactive scattering[33–36]. Yet, there remain many fields of physics and chemistry, where the effects of CIs on the collisional dynamics of molecules is not fully understood. Additional studies are required. We focus on the role of CIs in the hyperfine quenching of OH molecules in collisions with ultracold Sr atoms. It is our goal to answer the natural question whether a conical intersection in the collisional complex can influence the quenching dynamics of the free radical.

Results

Potential Surfaces involved in collisional dynamics.
The non-reactive collision physics of ^{88}Sr(^{1}S) colliding with the tightly-bound $v = 0$, $J = 3/2$ ro-vibrational ground-state of ^{16}O^{1}H(X$^2\Pi_{3/2}$) molecules is most conveniently described in three-dimensional Jacobi coordinates or vectors $\boldsymbol{R}$ and $\boldsymbol{r}$, where $R = |\boldsymbol{R}|$ is the separation between Sr and the center of mass of OH and $r = |\boldsymbol{r}|$ is the separation between O and H. It is also useful to define angle θ between $\boldsymbol{R}$ and $\boldsymbol{r}$. A schematic of the Jacobi coordinates is shown in Fig. 1b.

The relevant electronic structure of the tri-atomic system is well characterized by three non-relativisitic *diabatic* electronic potential surfaces: two shallow nearly-degenerate at large R van-der-Waals-bonded potentials labeled by $4\,^2A'(F^2\Pi)$ and $4\,^2A''(F^2\Pi)$ that dissociate to ground-state Sr(^{1}S) and OH($^2\Pi$) and one deep ionically-bound potential labeled by $1\,^2A'(X^2\Sigma^+)$. These surfaces are shown in Figs. 1 and 2. Where possible, we have estimated the uncertainties of our calculations. For example, in table 3 of our previous publication[30], in which we first presented the electronic states of SrOH, we compared the energies of three stretching and bending levels of the $1\,^2A'(X^2\Sigma^+)$ potential with the experimental values of Ref.[37]. The agreement is around 5 %. We also compared dissociation energies of our $1\,^2A'(X^2\Sigma^+)$ potential and its experimental value from[38]. Our dissociation energy of the (0,0,0) vibrational state is $D_0/hc = 33.3 \times 10^3$ cm^{-1}, which agrees well with the experimentally measured value of $32(1.4) \times 10^3$ cm^{-1}.

The potential surface of the ionically-bound $1\,^2A'(X^2\Sigma^+)$ state dissociates to an electronically-excited state of the Sr atom and the ground state OH(X$^2\Pi$) molecule. In our notation of states trimer symmetries $^2A'$ and $^2A''$ are further specified by $^2\Lambda^\pm$ labels in parenthesis. These describe the $C_{\infty v}$ symmetries of the electronic wavefunctions in co-linear geometries. It is convenient to denote trimer potentials by $C_{\infty v}$ labels as the equilibrium geometry of SrOH is linear with O in the center. In fact, the equilibrium separation between O and H is close to that of the $X^2\Pi$ ground-state potential of the OH dimer and the vibrational energy in the OH stretch is only 3 %
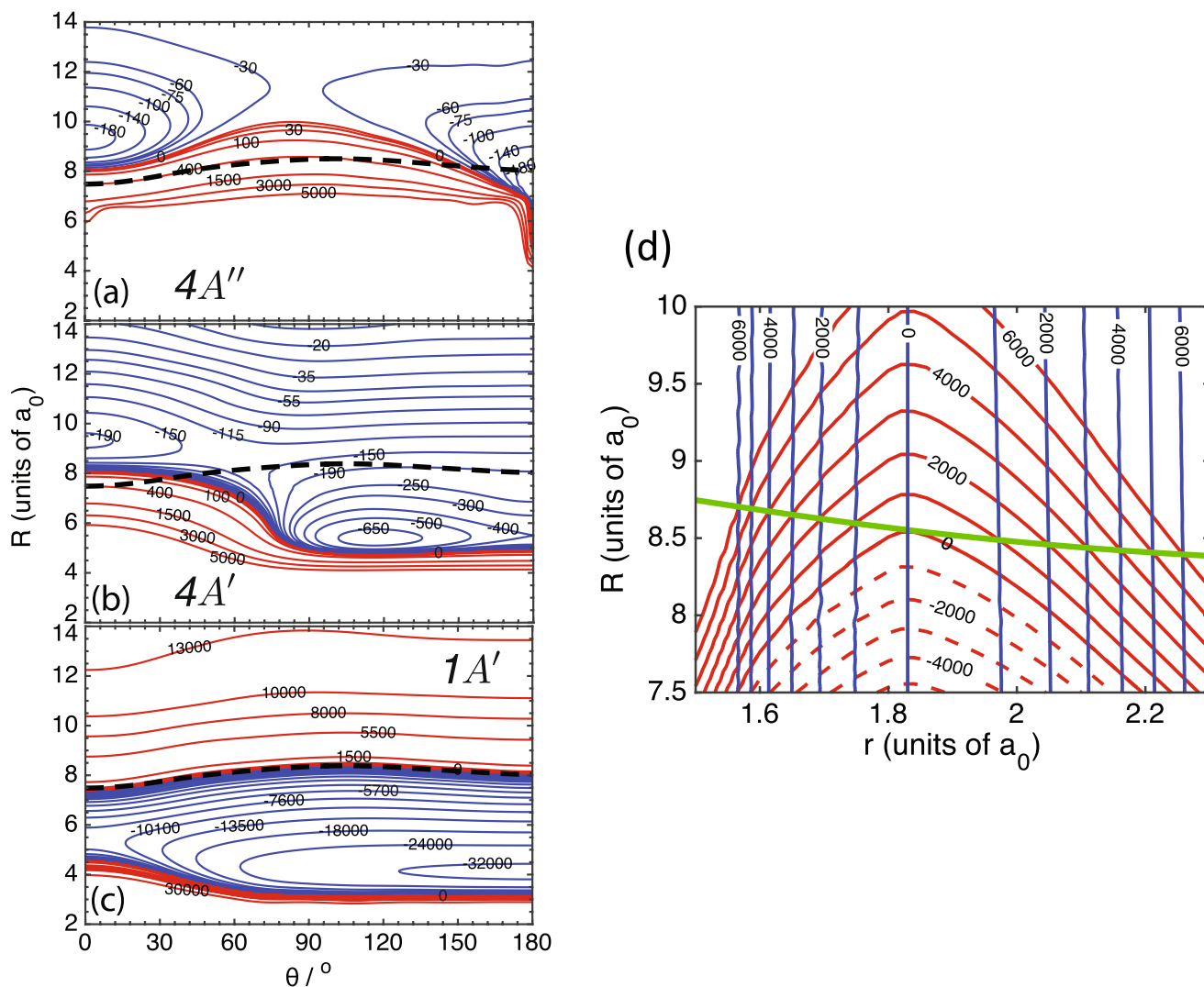
Figure 2. Contour plots of *diabatized* non-relativistic Sr + OH PESs. (**a–c**) Contour plots of $4\,^2A''(\mathrm{F}^2\Pi)$, $4\,^2A'(\mathrm{F}^2\Pi)$, and $1\,^2A'(\mathrm{X}^2\Sigma^+)$ states, respectively, as functions of Jacobi coordinates R and θ. Red and blue contours are labeled by potential energies in the units of cm^{-1}. The dashed black curve in each panel corresponds to locations where energies of the $1\,^2A'$ and $4\,^2A'$ states are equal. (**d**) Contour plot of the $1\,^2A'(\mathrm{X}^2\Sigma^+)$ (red curves) and $4\,^2A'(\mathrm{F}^2\Pi)$ (nearly-vertical blue curves) states as functions of Jacobi coordinates R and r for the collinear Sr-O-H arrangement with $\theta = 180°$. The seam of conical intersections is shown by the green curve. Contours are labeled by energies are in units of cm^{-1} and spaced by $1000\ \mathrm{cm}^{-1}$ for both potentials. The zero of energy is at the $\mathrm{Sr}(^1\mathrm{S}) + \mathrm{OH}(\mathrm{X}^2\Pi)$ dissociation limit. The OH separation is fixed at $r = 1.832a_0$.

larger than in the OH dimer. For our calculations it then also suffices to determine the three PESs for only a small range of OH separations r around the OH dimer equilibrium separation of $1.832a_0$, where a_0 is the Bohr radius.

Finally, trimer states $m\,^2A'$ are labeled by integer $m = 1, 2, \ldots$ and to a lesser extent by characters X and F in the parenthesis. The value m follows the energy ordering of $^2A'$ PESs near the trimer equilibrium geometry. As the diabatic $4\,^2A'$ and $4\,^2A''$ states are nearly degenerate at linear optimized geometry, the $^2A''$ is also denoted by $m = 4$ even though it is not the fourth state with this symmetry. The excited $2\,^2A'$ and $3\,^2A'$ electronic states have been omitted in our description of the Sr + OH collision. These potentials cross the $4\,^2A'(\mathrm{F}^2\Pi)$ potential at much smaller separations R and the effects of their couplings are expected to be smaller.

Figure 1a shows the two $^2A'$ electronic potentials at $\theta = 0°$ and $180°$, co-linear $C_{\infty v}$ geometries, as functions of separation R with $r = 1.832a_0$. The deeper and shallower of the two potentials correspond to the $1\,^2A'(\mathrm{X}^2\Sigma^+)$ and $4\,^2A'(\mathrm{F}^2\Pi)$ states, respectively. In these co-linear geometries the two states have conical intersections near $8a_0$. The energy of the CI for $\theta = 180°$ is lower than that of our entrance channel $\mathrm{Sr}(^1\mathrm{S}) + \mathrm{OH}(\mathrm{X}^2\Pi)$. The corresponding energy for $\theta = 0°$ is higher and thus classically forbidden. Figure 1b shows a schematic depiction of the Jacobi coordinates used in our model, whereas Fig. 1c describes Jacobi coordinates of the SrOH molecule in the optimized geometry.

We have determined these diabatic potentials and their couplings from *ab initio* non-relativistic coupled-cluster electronic-structure calculation of the SrOH PESs with single, double, and perturbative triple excitations
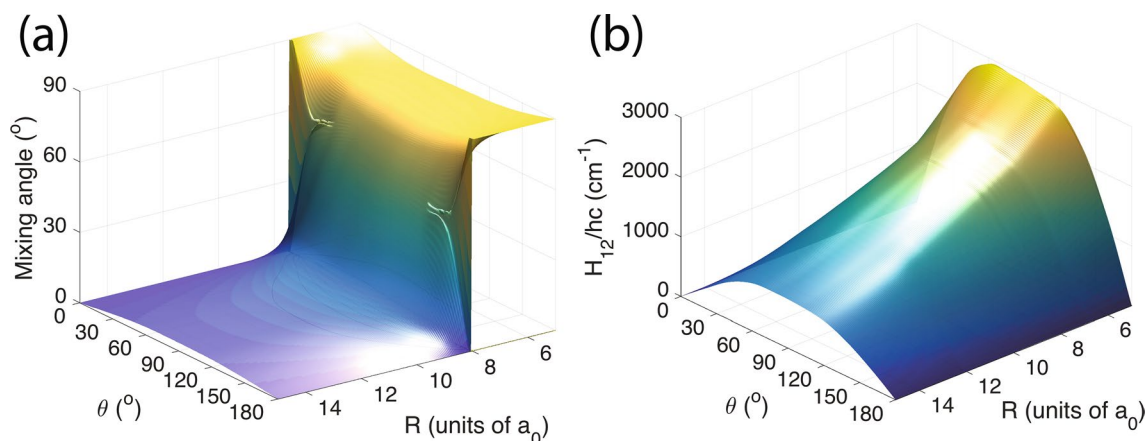
Figure 3. Mixing angle $\beta(R, r, \theta)$ (panel **a**) and coupling potential $H_{12}(R, r, \theta)$ (panel **b**) between the diabatic $1\,^2A'$ and $4\,^2A'$ states at $r = 1.832a_0$ as functions of Jacobi coordinates R and θ.

(CCSD(T)) and the equation-of-motion coupled cluster (EOM-CCSD(dT)) method described in detail in our previous study[30]. The procedures to diabatize the adiabatic potential energy surfaces, as determined by the non-relativistic electronic-structure calculations, have also been described in this reference.

Figure 2 shows a more quantitative view of the three diabatic potentials. In particular, the difference between the shallow potentials of the $4\,^2A''$ and $4\,^2A'$ states is apparent in panels (a) and (b) with their depths are around $hc \times 400\,\mathrm{cm}^{-1}$ and $hc \times 730\,\mathrm{cm}^{-1}$, respectively. In addition, the PES of the $4\,^2A''$ state is very shallow in the T-shape $\theta = 90°$ region, exhibiting a saddle point between the two collinear minima. The PES of $4\,^2A'$ is more attractive, allowing a closer approach of the Sr atom towards OH in a skewed geometry near $\theta = 120°$. The $4\,^2A'$ state has two saddle points: one collinear with $\theta = 180°$ and one around $\theta = 60°$. The $1\,^2A'$ potential is very deep and shown in Fig. 2c. In all panels we have indicated the curve where the $1\,^2A'$ and $4\,^2A'$ states have the same energy. On this curve conical intersections occur at $\theta = 0°$ and $180°$.

For heteronuclear tri-atomic molecules conical intersections are not isolated molecular geometries, but form a one-dimensional *seam*. The molecule can undergo nonadiabatic passage or transitions at any point of this seam. In SrOH the seam between the $1\,^2A'$ and $4\,^2A'$ potentials lies in the (R, r) plane with angle θ at either $0°$ or $180°$. Figure 2d shows the $1\,^2A'$ and $4\,^2A'$ potentials in this plane for $\theta = 180°$ as well as the seam located between $R = 8.3a_0$ and $8.7a_0$. The equal-energy contours of the $4\,^2A'$ state are nearly independent of r. As this diabatic state dissociates to $\mathrm{Sr}(^1\mathrm{S}) + \mathrm{OH}(^2\Pi)$ for large R and the $\mathrm{OH}(^2\Pi)$ state has a zero-point energy of nearly $hc \times 2000$ cm^{-1}, only a limited region of r around $1.832a_0$ is relevant. For the diabatic $1\,^2A'$ state the contours are curved in the (R, r) plane with the largest R value very close to the OH equilibrium separation. In fact, the curvature at the equilibrium separation is almost independent of contour especially for contours with energy less than that of the $\mathrm{Sr}(^1\mathrm{S}) + \mathrm{OH}(^2\Pi)$ limit. Equivalently, except for an energy off set, the $1\,^2A'$ potential as function of r close to $1.832a_0$ is nearly independent of R. In fact, as noted before the OH separation and zero-point energy of the OH stretch in the SrOH trimer at its equilibrium geometry (not shown in Fig. 2d) are close to that of the OH dimer. We will then assume that in the collision OH vibrational motion in the $1\,^2A'$ state is limited to a small range of r around $1.832a_0$.

We require diabatic PESs for use in coupled-channels calculations of the Sr + OH collision. Only adiabatic PESs, however, are available from electronic structure calculations, here provided by the MOLPRO and Q-CHEM programs[39,40]. In addition, we computed the mixing angles $\beta(R, r, \theta)$ for the adiabatic $^2A'$ states by the DDR procedure within the MRCI method[30]. The corresponding adiabatic states and potentials were transformed into diabatic states and potentials described in the previous subsection, so that the problematic avoided crossings near and degenerate singular part at the CI seam are "removed"[41]. By construction diabatic states are independent of the Jacobi coordinates near the CI and coupled by coupling potentials $H_{1,2}(R, r, \theta)$ between diabatic states 1 and 2. Specifically, near the CI seam between the $1\,^2A'$ and $4\,^2A'$ states we first computed a 2×2 orthogonal matrix $\mathbf{O}(R, r, \theta)$, parameterized by mixing angle $\beta(R, r, \theta)$, to transfer between the adiabatic and diabatic states. From the orthogonal matrix the coupling function can be easily constructed. For details see Ref.[30].

Figure 3 shows the mixing angle $\beta(R, r, \theta)$ and coupling potential $H_{12}(R, r, \theta)$ between $1\,^2A'$ and $4\,^2A'$ diabatic states as a function of Jacobi coordinates R and θ. At the CI the mixing angle changes rapidly from $90°$ to $0°$. The value of the coupling function is zero at $\theta = 0°$ and $180°$ and has a maximal strength of approximately $3300\,\mathrm{cm}^{-1}$ near $\theta = 90°$ and $R = 8.5a_0$. For large R the coupling relatively fast decreasing.

Dynamics in the vicinity of a conical intersection. To assess the collision of $^{88}\mathrm{Sr}(^1\mathrm{S})$ with the rovi-brational ground state of $^{16}\mathrm{O}^1\mathrm{H}(\mathrm{X}^2\Pi)$ it is convenient to first introduce relevant energy correlation diagram in Fig. 4. It illustrates the reaction pathway of our system, which highlights stationary points (minima or saddle points) in the PESs. The pathway is based on *ab-initio* calculations described in Ref.[30]. The reaction to form $\mathrm{SrO}(\mathrm{X}^1\Sigma^+) + \mathrm{H}(^2\mathrm{S})$ is endothermic by $hc \times 2890\,\mathrm{cm}^{-1}$ when accounting for the significant difference in zero point energy of OH and SrO. The entrance-channel van-der-Waals interaction between Sr and OH creates a rela-
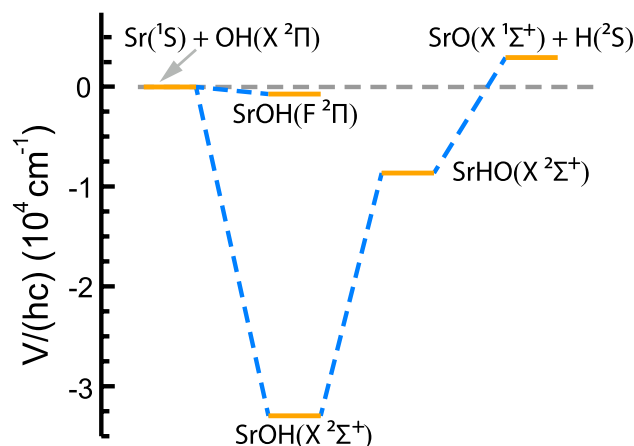
Figure 4. Collision or reaction path of the Sr + OH system. The Sr(^{1}S) + OH(X$^2\Pi$) entrance channel is shown on the left. Its energy is the zero of energy in the graph. The SrO(X$^1\Sigma^+$) + H(^{2}S) channel shown on the right is endothermic by $hc \times 2890$ cm^{-1} and includes the difference in zero-point energy of OH and SrO. The three states with negative energies in between are trimer states with collinear geometries that are (local) minima of the 1 $^2A'$(X$^2\Sigma^+$) and 4 $^2A'$(F$^2\Pi$) electronic potentials as indicated. Electronic energies are taken from *ab initio* CCSD(T) calculations of Ref.[30].
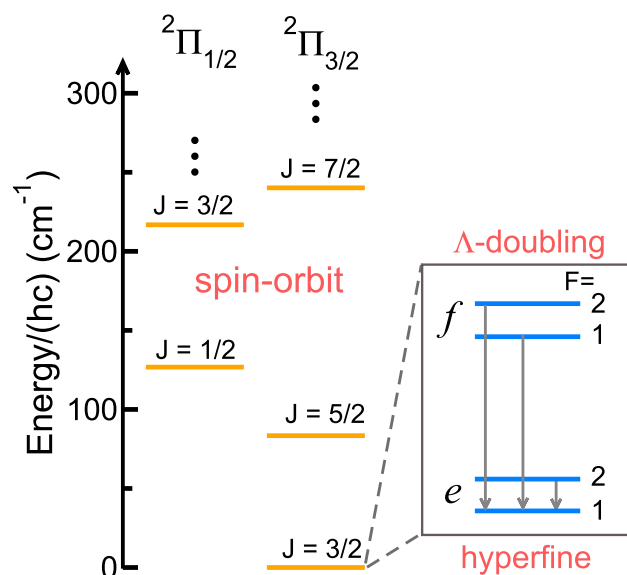

Figure 5. Energies of the $v = 0$ vibrational level of the X$^2\Pi_\Omega$ state of ^{16}O^{1}H. The left-hand side of the figure shows the $\Omega = 1/2$ and 3/2 spin-orbit splitting as well as a rotational progression in J. A blowup of the less than $hc \times 0.1$ cm^{-1} Λ-doubling (labeled by e and f) and hyperfine splittings ($F = 1$ and 2) of the energetically-lowest $J = 3/2$ level are shown on the right. Hyperfine splittings are due to coupling between the nuclear spin and electronic motion. Arrows indicate the relevant collision-induced transitions between hyperfine components within ^{16}O^{1}H. Their transition energies are given in the text. The zero of energy is at the energetically-lowest hyperfine state.

tively shallow $hc \times 730$ cm^{-1} deep well in the 4 $^2A'$(F$^2\Pi$) collisional complex that is non-adiabatically coupled to the $hc \times 33\,300$ cm^{-1} deep well in the 1 $^2A'$(X$^2\Sigma^+$) collisional complex.

The relevant energy diagram of the $v = 0$ vibrational state of ^{16}O^{1}H(X$^2\Pi$) is shown in Fig. 5 based on spectroscopic data of Ref.[42]. The energy spacing between the $v = 0$ and $v = 1$ vibrational levels of this state is about $hc \times 3570$ cm^{-1} (not shown). The $v = 0$ level has $^2\Pi_{\Omega=1/2}$ and $^2\Pi_{\Omega=3/2}$ spin-orbit components separated by just over $hc \times 100$ cm^{-1}. The energetically-lowest rotational level is a $J = 3/2$ state. The nuclear spin $\boldsymbol{I}$ of the hydrogen atom in ^{16}OH leads to hyperfine splittings of the ground state rotational levels into components labeled by quantum number F, where $\boldsymbol{F} = \boldsymbol{J} + \boldsymbol{I}$ is the total angular momentum of ^{16}OH. Finally, the $\Omega = 3/2$ state is split into opposite parity states e and f due to a weak non-adiabatic coupling, called Λ-doubling. The transition
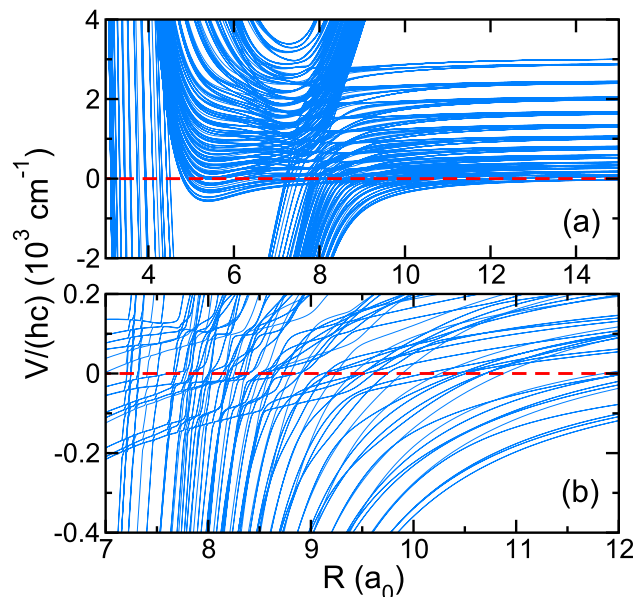
Figure 6. Adiabatic potential energies with $F_{tot} = 2$ and even parity of the ^{88}Sr with $v = 0, J = 3/2$ ^{16}OH($^2\Pi_{3/2}$) collision as functions of R. Panels (**a,b**) show different energy scales of the same potentials. OH rotational states up to $J = 25/2$ are included. The zero of energy is at the energetically-lowest $F = 2$ hyperfine state of OH.

energies between hyperfine and Λ-doubling states of the $v = 0, J = 3/2, \Omega = 3/2$ level of ^{16}OH(X$^2\Pi$) relevant for this paper are

$$\Delta E(|f; F = 2\rangle - |e; F' = 1\rangle)/hc = 0.057 \, \text{cm}^{-1},$$
$$\Delta E(|f; F = 1\rangle - |e; F' = 1\rangle)/hc = 0.055 \, \text{cm}^{-1},$$
$$\Delta E(|e; F = 2\rangle - |e; F' = 1\rangle)/hc = 0.0018 \, \text{cm}^{-1},$$

where in kets $|e/f; F\rangle$ and $|e/f; F'\rangle$ we omitted labels for the electronic and ro-vibrational state of ^{16}OH for clarity.

We have developed a coupled-channels model to calculate atom-dimer quenching rate coefficients for ^{88}Sr $+^{16}$O^{1}H collision energies below $hc \times 10^{-2} \, \text{cm}^{-1}$ or $k_B \times 10$ mK, where k_B is the Boltzmann constant, in a rigid rotor approximation for OH. That is, under the assumption that the OH stretch in SrOH is not excited in the Sr + OH collision. The model includes the three diabatic non-relativistic $^2A'$ and $^2A''$ trimer potential surfaces and their couplings as well as the spin-orbit, rotational, Λ-doubling, and hyperfine interactions in the OH dimer. The vibrational wavefunction of the OH stretch is that of the $v = 0$ eigenstate of the OH dimer for both the $^2A'$ and $^2A''$ symmetries. As discussed in the previous section this assumption is mainly justified by the observation that near the equilibrium geometry of the $1\,^2A'(X^2\Sigma^+)$ state the vibrational energy of the OH stretch is close to that in the dimer. Secondly, the depth of the potentials in the $4\,^2A'(F^2\Pi)$ and $4\,^2A''(F^2\Pi)$ states is less than the ground vibrational spacing of the OH(X$^2\Pi$) dimer.

Hence, we expand that the six-dimensional scattering wavefunction as a superposition of products of spherical harmonics with relative orbital angular momentum ℓ in the orientation $\hat{R}$ of coordinate R and rigid-rotor $v = 0$ ro-vibrational states for OH in r, such that the total trimer angular momentum $F_{tot} = \ell + F$ and parity are conserved. For this system negative (positive) parity correspond to states or channels with odd(even) value for partial wave ℓ. Details about the basis set are given in Methods.

The expansion leads to coupled Schrödinger equations in separation R with potential matrix element $U_{ij}(R)$ between basis set elements i and j. We have numerically solved the differential equations and for $R \to \infty$ construct rate coefficients from the solutions. The coupled-channels calculations are computationally demanding as a large number of OH rotational channels J need to be included. The $^2A'$ and $^2A''$ potentials have strong angular anisotropies that couple many OH spin-orbit, rotational and hyperfine states. In the remainder of this paper we will study elastic and inelastic rate coefficients of Sr and OH in states $|f; F = 1, 2\rangle$ or $|e; F = 1, 2\rangle$ states, defined in Fig. 5. In addition, we intend to show how the conical intersection influences the outcome of the collision. This is achieved by switching the CI "off" by simply setting $H_{12}(R, r, \theta) = 0$.

Figure 6 shows the $F_{tot} = 2$ and even parity eigenvalues of matrix $U_{ij}(R)$ as functions of R at two energy and length scales. We have included the energetically-lowest 12 rotational states of the $v = 0$ X$^2\Pi_{1/2}$ and $v = 0$ X$^2\Pi_{3/2}$ states of ^{16}OH. These eigenvalues are also called adiabatic potentials, but now in the sense that only motion in the radial R direction is considered slow. Most importantly, we observe that the density of collisional channels is high with spacings much smaller than the coupling strength $H_{12}(R, r, \theta)$ providing by the CI. In fact, near $R = 8a_0$ in both Figs. 6a, b a "bundle" of nearly-vertical curves avoids, in a complicated manner, a bundle of
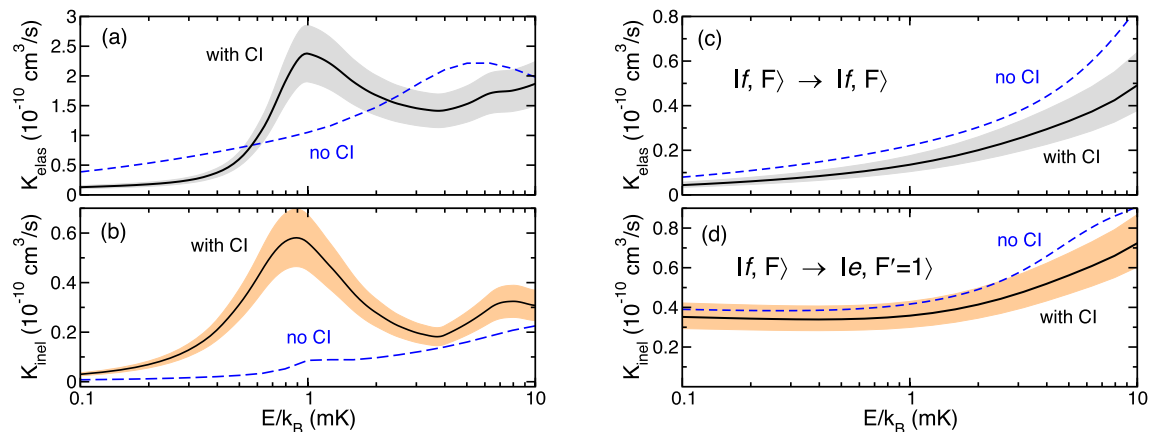
Figure 7. Collision energy dependence of the total elastic, panels (**a,c**), and inelastic, panels (**b,d**), rate coefficients for ^{88}Sr + ^{16}O^{1}H with $v = 0, J = 3/2$ ^{16}OH(X$^2\Pi_{3/2}$). Solid and dashed lines indicate results of coupled-channels calculations with and without conical intersection between $1\,^2A'$ and $4\,^2A'$ potentials, respectively. OH $v = 0$ rotational states up to $J = 25/2$ are included. The grey and orange bands reflect our estimate of the one-standard deviation uncertainty of the rate coefficient due to our inability to include all rotational states of OH when the CI is included in the calculations. Panels (**a,b**) show total elastic and partial inelastic hyperfine quenching rate coefficients for OH in its $|e; F = 2\rangle$ hyperfine state, whereas panels (**c,d**) show rate coefficients for OH in its $|f; F = 1\rangle$ and $|f; F = 2\rangle$ hyperfine states. Rate coefficients for $|f; F = 1\rangle$ and $|f; F = 2\rangle$ are indistinguishable on the scale of the figure.

nearly-horizontal curves. The former bundle is due to the $1\,^2A'(\mathrm{X}^2\Sigma^+)$ state. The latter is due to both $4\,^2A'(\mathrm{F}^2\Pi)$ and $4\,^2A''(\mathrm{F}^2\Pi)$ states. Their avoided crossings are due to the CI.

Figure 7 shows the total elastic and hyperfine quenching inelastic rate coefficients obtained from coupled-channels calculations as a function of collision energy E for OH in the hyperfine entrance channel $|e; F = 2\rangle$, $|f; F = 2\rangle$, and $|f; F = 1\rangle$. Quenching leads to OH molecules in state $|e; F' = 1\rangle$. For these calculations, we have included the energetically-lowest 12 rotational states of the $v = 0\,\mathrm{X}^2\Pi_{1/2}$ and $v = 0\,\mathrm{X}^2\Pi_{3/2}$ states of OH. Collisions with partial wave quantum numbers up to $\ell = 8$ contribute to our entrance channels and collision energies $E/k_\mathrm{B} < 10\,\mathrm{mK}$. Rate coefficients calculated when the coupling near the CI is switched on and off are shown.

Figure 7a,b show elastic and inelastic hyperfine quenching rate coefficients when OH is prepared in hyperfine entrance channel $|e; F = 2\rangle \rightarrow |e; F' = 1\rangle$. Both rate coefficients have a resonance feature with a maximum value near $E = k_\mathrm{B} \times 1\,\mathrm{mK}$ but only when the coupling between the $1\,^2A'$ and $4\,^2A'$ states is switched on. This resonance is much weaker when the coupling is turned off. We observe that for both cases the elastic rate coefficients are about five time larger than the inelastic ones. Figure 7c,d show elastic and inelastic hyperfine quenching rate coefficients when OH is prepared in either hyperfine entrance channel $|f; F = 2\rangle \rightarrow |e; F' = 1\rangle$ or $|f; F = 1\rangle \rightarrow |e; F' = 1\rangle$. The rate coefficients are indistinguishable on the scale of the figure.

Analysis, based on studying the contributions from individual F_tot and parity channels, has shown that the resonances that appear in Fig. 7a,b are due to a shape resonance behind and tunneling through a $\ell = 1$, p-wave centrifugal barrier leading to quantum enhanced scattering. Similarly, the broader resonances near $E = k_\mathrm{B} \times 8\,\mathrm{mK}$ with CI coupling and near $E = k_\mathrm{B} \times 5\,\mathrm{mK}$ without CI coupling are found to be due to $\ell = 2$, d-wave shape resonances.

Figure 8 explains the analysis of the resonances. The figure shows the relevant $F_\mathrm{tot} = 1$ adiabatic eigenvalues of matrix $U_{ij}(R)$ for large R close to the OH $|e; F = 1\rangle$ and $|e; F = 2\rangle$ dissociation limits. Panels (a) and (b) show potentials for even and odd partial wave channels, respectively. On these energy and length scales centrifugal barriers for the p and d wave channels are visible with approximate barrier heights of about $k_\mathrm{B} \times 1\,\mathrm{mK}$ and $k_\mathrm{B} \times 10\,\mathrm{mK}$, respectively. Higher partial wave entrance channels have even higher barriers and do not significantly contribute to rate coefficients for collision energies below $k_\mathrm{B} \times 10\,\mathrm{mK}$. These barriers are not shown in the figure even though the corresponding channels are included in our coupled channels calculations. For our $|e; F = 2\rangle$ entrance channel and $F_\mathrm{tot} = 1$ the $\ell = 0$ state does not exist. (The s-wave channel for the Sr + OH $|e; F = 2\rangle$ collision only occurs when $F_\mathrm{tot} = 2$.) The heights or tops of the p- and d-wave barriers are thus consistent with the two resonances when the coupling between $1\,^2A'$ and $4\,^2A'$ states is turned on. The location of the resonance at $E = k_\mathrm{B} \times 5\,\mathrm{mK}$ when the coupling is turned off can only be explained by the d-wave centrifugal barrier for the $|e; F = 1\rangle$ exit channel, whose dissociation energy is about $k_\mathrm{B} \times 2.5\,\mathrm{mK}$ lower in energy than that of the $|e; F = 2\rangle$ entrance channel.

Finally, we have to note that with current computing capabilities first-principle calculations can not be fully converged with respect to the number of OH rotational states J included in our coupled-channels calculations when 100% of the coupling between the $1\,^2A'$ and $4\,^2A'$ states is turned on. These uncertainties are indicated in Fig. 7 by colored bands and estimated from our results of two consecutive calculations of the elastic and inelastic rates with $J = 25/2$ and $27/2$. The difference between the rate coefficients for $J = 25/2$ and $27/2$ is taken as the one standard-deviation uncertainty. We have reached convergence when the coupling between the potential surfaces is turned off. Figure 7 also show that the inelastic rate coefficients obey the Wigner threshold law and approach a finite value in limit of zero collision energy.
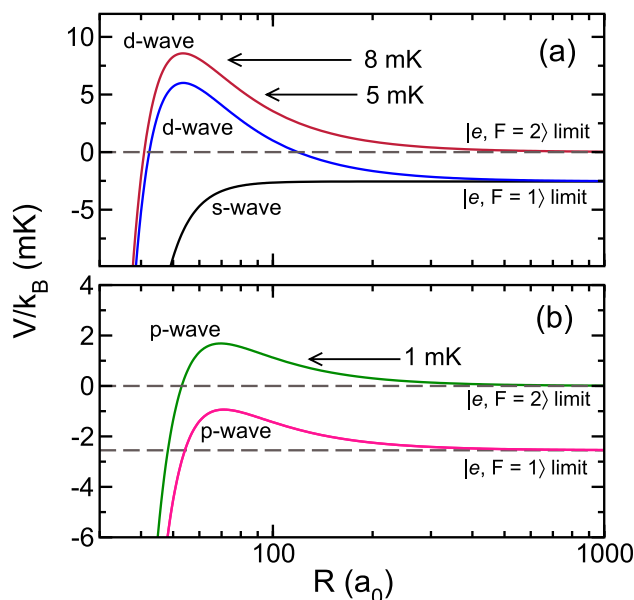
Figure 8. Centrifugal *s*, *p*, and *d*-wave barriers as functions of *R* for the $F_{\text{tot}} = 1$ ^{88}Sr + ^{16}OH collision near the ^{16}OH $|e; F = 1\rangle$ and $|e; F = 2\rangle$ hyperfine thresholds based on the adiabatic potentials in the coupled-channels calculations. Panels (**a**,**b**) show potentials for even and odd valued partial waves, respectively. The zero of energy is at the $|e; F = 2\rangle$ ^{16}OH threshold. Arrows with collision energies E/k_B in mK indicate the locations of collisional resonances in Fig. 7.

Discussion

We have created computational tools to compute elastic and quenching rate coefficients of the ultracold ^{88}Sr + ^{16}OH collision in the presence of nonadiabatic coupling between potential surfaces. These tools allowed us to treat the electronic structure and the nonadiabatic nuclear dynamics, dominated by conical intersections, with quantum chemical and quantum dynamical methods. In particular, we have performed state-of-the-art calculations of non-reactive collisional dynamics of hydroxyl with Sr based on three electronic potential-energy surfaces using only a localized region of the tri-atomic nuclear coordinate space.

An important aspect of the investigation has been to answer the question whether conical intersections affect the quenching of the hyperfine levels of the ultracold ground-state OH molecule. We therefore calculated collisional quenching rates under conditions where the conical intersection can be switched on and off. This was achieved by using diabatic electronic basis functions. The results have shown that at low collision energy the conical intersection has important consequences for the collisional properties of OH. Specifically, when OH is prepared in one of its energetically-lowest hyperfine states shape resonances can be observed, which change their location or are absent when the coupling is turned off.

Methods

Basis set: The ultracold non-reactive ^{88}Sr + ^{16}OH scattering wave function $|\Psi\rangle$ is expanded in ^{16}OH molecular eigenstates using Jacobi coordinates $\boldsymbol{R}$ and $\boldsymbol{r}$ defined in Fig. 1. That is,

$$\langle \boldsymbol{R}, \boldsymbol{r}|\Psi\rangle = \sum_i F_i(R) \, \langle \hat{\boldsymbol{R}}, \boldsymbol{r}|\psi_i\rangle, \tag{1}$$

where index *i* labels basis states or channels $|\psi_i\rangle$. The sum over channels is constrained to conserve total angular momentum of the trimer $\boldsymbol{F}_{\text{tot}}$ and parity $p_{\text{tot}} = \pm 1$.

Channel states $|\psi_i\rangle$ are given by

$$\langle \hat{\boldsymbol{R}}, \boldsymbol{r}|\psi_i\rangle = \sum_{mM} C^{F_{\text{tot}}M_{\text{tot}}}_{\ell m, FM} \, Y_{\ell m}(\hat{\boldsymbol{R}}) \, \langle \boldsymbol{r}|\varphi_{\tau;FM;p}\rangle, \tag{2}$$

where $C^{jm}_{j_1 m_1, j_2 m_2}$ are Clebsch–Gordan coefficients, $Y_{\ell m}(\hat{\boldsymbol{R}})$ are spherical harmonic functions of the orbital angular momentum of partial wave ℓ, and $|\varphi_{\tau;FM;p}\rangle$ describe electronic and OH ro-vibrational states with combined angular momentum $\boldsymbol{F}$ and parity p. Label τ is used to further describe these states. Projection quantum numbers M_{tot}, m, and M of $\boldsymbol{F}_{\text{tot}}$, $\boldsymbol{\ell}$, and $\boldsymbol{F}$, respectively, are given with respect to a space-fixed laboratory axis. Here, $\boldsymbol{F}_{\text{tot}} = \boldsymbol{\ell} + \boldsymbol{F}$, parity $p_{\text{tot}} = (-1)^{\ell} p$.

In principle, states $|\varphi_{\tau;FM;p}\rangle$ form a complete set of electronic and OH ro-vibrational states. In order to make the computations tractable, however, we must introduce various approximations. The first is that the electronic wavefunctions are restricted to be the non-relativistic *diabatic* states $|1\,^2A'(X^2\Sigma^+)\rangle$, $|4\,^2A'(F^2\Pi)\rangle$, and $|4\,^2A''(F^2\Pi)\rangle$, defined in the main text. These diabatic states are assumed to be independent of *R*, *r*, and θ

(an approximation already implicit in the notation used in Eqs. 1 and 2.) We further assume that these trimer electronic wavefunctions are given by simple products of $Sr(^1S)$ and either $^2\Pi$ and $^2\Sigma^+$ ^{16}OH dimer electronic wavefunctions. That is, $|4\,^2A'(F\,^2\Pi)\rangle$ and $|4\,^2A''(F\,^2\Pi)\rangle$ are superpositions of $|Sr(^1S)\rangle|OH(X\,^2\Lambda)\rangle$ with projection quantum number $\Lambda = \pm\Pi$ or ± 1 and $|1\,^2A'(X^2\Sigma^+)\rangle \rightarrow |Sr(^1S)\rangle|OH(^2\Sigma^+)\rangle$ (The state has projection $\Lambda = \Sigma$ or 0), re-enforcing the usefulness of labeling trimer electronic states with $C_{\infty v}$ symmetries at collinear geometries.

Secondly, the vibrational motion of the OH stretch is limited to that of the $v = 0$ state of ^{16}OH$(X^2\Pi)$. This approximation relies on the observations that the $4\,^2A'(F^2\Pi)$ and $4\,^2A''(F^2\Pi)$ potentials are less deep than the vibrational spacing of OH$(X^2\Pi)$ and that near the conical intersections of the $|1\,^2A'(X^2\Sigma^+)\rangle$ and $|4\,^2A'(F^2\Pi)\rangle$ states the r dependence of the $1\,^2A'(X^2\Sigma^+)$ potential, except for a constant energy offset, is nearly independent of R. Near the equilibrium geometry of the $1\,^2A'(X^2\Sigma^+)$ potential the vibrational energy in the OH stretch is within 3 % of that of the OH$(X^2\Pi)$ dimer.

Spin-orbit interactions and OH rotation are included based on our assumption that trimer electronic states are separable and determined by those in the OH dimer. Then spin-orbit interactions in the $|1\,^2A'(X^2\Sigma^+)\rangle$ state are absent while those in the $|4\,^2A'(F^2\Pi)\rangle$ and $|4\,^2A''(F^2\Pi)\rangle$ states correspond to those in the OH$(X^2\Pi)$ dimer. States represented by $^2\Sigma^+_{\Omega=1/2}$ and $^2\Pi_{\Omega=1/2,3/2}$ with OH electronic angular momentum projection $\Omega = 1/2$ and $3/2$ on the internuclear axis of ^{16}OH are formed. The rotation, coriolis and hyperfine interactions, as well as Λ-doubling in SrOH are similarly based on those in OH. In fact, these latter interactions weakly mix $^2\Pi_{\Omega=1/2}$ and $^2\Pi_{\Omega=3/2}$ states as well as mix electron-rotational angular momentum states J. See Refs.[43,44] for a discussion of symmetries of and the spin-orbit, hyperfine, Λ-doublet interactions in OH.

In practice, the relevant states are

$$\langle \boldsymbol{r}|\varphi_{\tau;FM;p}\rangle = \varphi_{v=0,J\Omega}(r)$$
$$\times \sum_{M_J M_I} C^{FM}_{JM_J,IM_I} \langle \hat{\boldsymbol{r}}|^2\Lambda_\Omega, JM_J\Omega; p\rangle|IM_I\rangle , \tag{3}$$

where radial functions $\varphi_{v=0,J\Omega}(r)$ are $v = 0, J$ OH$(X^2\Pi_\Omega)$ rotational levels, obtained by numerical diagonalization of the OH Hamiltonian excluding the coriolis, hyperfine, Λ-doubling interactions[43], and OH electron-rotational states $|^2\Lambda_\Omega, JM_J\Omega; p\rangle$ are

$$\langle \hat{\boldsymbol{r}}|^2\Lambda_\Omega, JM_J\Omega; p\rangle = |Sr(^1S)\rangle \frac{1}{\sqrt{2}}\Big\{ \theta^J_{M_J,\Omega}(\hat{\boldsymbol{r}})|OH(^2\Lambda_\Omega)\rangle$$
$$+ (-1)^{J+2\Omega+1/2} p\, \theta^J_{M_J,-\Omega}(\hat{\boldsymbol{r}})|OH(^2\Lambda_{-\Omega})\rangle \Big\} \tag{4}$$

with

$$\theta^J_{M_J,\Omega}(\hat{\boldsymbol{r}}) = \sqrt{\frac{2J+1}{4\pi}} D^{J*}_{M_J,\Omega}(\alpha,\beta,\gamma=0) . \tag{5}$$

Here, operator $\boldsymbol{J}$ is the electron-rotational angular momentum of ^{16}OH with quantum number J and projections M_J and Ω along the laboratory axis and ^{16}OH axis $\boldsymbol{r}$, respectively. Functions $D^J_{M,\Omega}(\alpha,\beta,\gamma)$ are Wigner rotation functions with Euler angles α, β, and γ that specify the orientation of OH and, thus, $\boldsymbol{r}$ in our space-fixed coordinate system. For the ^{16}OH electronic wavefunctions $|OH(^2\Lambda_\Omega)\rangle$ we have $\Lambda = \Sigma$ and Π (or 0 and 1). Finally, the ket $|IM_I\rangle$ describes the nuclear spin wavefunction of H with $M_I = \pm 1/2$ and total ^{16}OH angular momentum $\boldsymbol{F} = \boldsymbol{J} + \boldsymbol{I}$. Consistent with our approximations we have ignored the electronic state dependence of $\varphi_{v=0,J\Omega}(r)$. Historically, e states are states with $p = (-1)^{J-1/2}$ while f states are states with $p = (-1)^{J+1/2}$. In summary, index i in Eq. 1 represents labels and quantum numbers $^2\Lambda_\Omega; p, [(JI)F, \ell]F_{tot}M_{tot}; p_{tot}$. Similarly, τ in Eq. 2 represents $^2\Lambda_\Omega; JI$. Reference[45] gives details of the required angular momentum algebra for a simpler case.

Finally, the radial wave functions $F_i(R)$ are channel components and only depend on the separation R between the center of mass of the molecule and the atom. They are determined from numerically integrating the coupled radial Schrödinger equations

$$\left\{ -\frac{\hbar^2}{2\mu}\frac{d^2}{dR^2} + \boldsymbol{U}(R) \right\}\boldsymbol{F}(R) = E\,\boldsymbol{F}(R) \tag{6}$$

for total energy E from $R = 0$ to $R \rightarrow \infty$. Here, vector $\boldsymbol{F}(R)$ contains all $F_i(R)$ and μ is the reduced mass of the atom-molecule system. The first term in curly brackets on the left hand side of this equation is a diagonal matrix for the radial kinetic energy (the same for each channel), while the second term $\boldsymbol{U}(R)$ is the potential matrix with elements $U_{ij}(R) = \langle\psi_i|U|\psi_j\rangle$ between channels i and j and includes the three *diabatic* potentials $V(R,r,\theta)$ and their couplings, the rotation energy of Sr around OH, $\hbar^2\boldsymbol{\ell}/(2\mu R^2)$, as well as the spin-orbit, rotational and hyperfine energies of the $v = 0$ vibrational level of OH. In fact, $\boldsymbol{U}(R)$ is anisotropic, orientation dependent as channels with different values for ℓ or m are coupled. We limit the number of channel components by only including ^{16}OH rotational states $J \leq 25/2$.

At large separations $\boldsymbol{U}(R)$ is an "almost" diagonal matrix. For the basis in Eq. 3 weak couplings by OH coriolis, hyperfine and Λ-doubling interactions persist and mix states with different values of Ω and J. Hence, in order to compute scattering amplitudes and rate coefficients we first calculate the orthonormal matrix that diagonalizes $\boldsymbol{U}(R)$ at a large R and transform $\boldsymbol{F}(R)$ into the basis in which $\boldsymbol{U}(R)$ is diagonal.

Data availability
All data generated or analysed during this study are available upon request.

References

1. Alyabyshev, S. V., Lemeshko, M. & Krems, R. V. Sensitive imaging of electromagnetic fields with paramagnetic polar molecules. *Phys. Rev. A* **86**, 013409 (2012).
2. DeMille, D. Quantum computation with trapped polar molecules. *Phys. Rev. Lett.* **88**, 067901 (2002).
3. Ni, K.-K., Rosenband, T. & Grimes, D. D. Dipolar exchange quantum logic gate with polar molecules. *Chem. Sci.* **9**, 6830–6838 (2018).
4. Sawant, R. *et al.* Ultracold polar molecules as qudits. *New J. Phys.* **22**, 013027 (2020).
5. Gorshkov, A. V. *et al.* Quantum magnetism with polar alkali-metal dimers. *Phys. Rev. A* **84**, 033619 (2011).
6. Moses, S. A., Covey, J. P., Miecnikowski, M. T., Jin, D. S. & Ye, J. New frontiers for quantum gases of polar molecules. *Nat. Phys.* **13**, 13–20 (2017).
7. Hudson, J. J. *et al.* Improved measurement of the shape of the electron. *Nature* **473**, 493–496 (2011).
8. Baron, J. *et al.* Order of magnitude smaller limit on the electric dipole moment of the electron. *Science* **343**, 269–272 (2014).
9. Kozyryev, I. & Hutzler, N. R. Precision measurement of time-reversal symmetry violation with laser-cooled polyatomic molecules. *Phys. Rev. Lett.* **119**, 133002 (2017).
10. Safronova, M. S. *et al.* Search for new physics with atoms and molecules. *Rev. Mod. Phys.* **90**, 025008 (2018).
11. Balakrishnan, N. Perspective: Ultracold molecules and the dawn of cold controlled chemistry. *J. Chem. Phys.* **145**, 150901 (2016).
12. Hu, M.-G. *et al.* Direct observation of bimolecular reactions of ultracold KRb molecules. *Science* **366**, 1111–1115 (2019).
13. Hu, M.-G. *et al.* Product-state control of ultracold reactions via conserved nuclear spins. arXiv preprint arXiv:2005.10820 (2020).
14. Lev, B. L. *et al.* OH hyperfine ground state: From precision measurement to molecular qubits. *Phys. Rev. A* **74**, 061402 (2006).
15. Hudson, E. R., Lewandowski, H. J., Sawyer, B. C. & Ye, J. Cold molecule spectroscopy for constraining the evolution of the fine structure constant. *Phys. Rev. Lett.* **96**, 143004 (2006).
16. Kozlov, M. G. Λ-doublet spectra of diatomic radicals and their dependence on fundamental constants. *Phys. Rev. A* **80**, 022118 (2009).
17. Fast, A., Furneaux, J. E. & Meek, S. A. Precision spectra of $A^2\Sigma^+$, $v' = 0 \leftarrow X^2\Pi_{3/2}$, $v'' = 0$, $J'' = 3/2$ transitions in ^{16}OH and ^{16}OD. *Phys. Rev. A* **98**, 052511 (2018).
18. Green, S. Interstellar chemistry: Exotic molecules in space. *Annu. Rev. Phys. Chem.* **32**, 103–138 (1981).
19. Bochinski, J. R., Hudson, E. R., Lewandowski, H. J., Meijer, G. & Ye, J. Phase space manipulation of cold free radical OH molecules. *Phys. Rev. Lett.* **91**, 243001 (2003).
20. Yusef-Zadeh, F., Wardle, M., Rho, J. & Sakano, M. OH (1720 MHz) masers and mixed-morphology supernova remnants. *Astrophys. J.* **585**, 319 (2003).
21. Rex, M. *et al.* A tropical west pacific OH minimum and implications for stratospheric composition. *Atmos. Chem. Phys.* **14**, 4827–4841 (2014).
22. Stuhl, B. K. *et al.* Evaporative cooling of the dipolar hydroxyl radical. *Nature* **492**, 396–400 (2012).
23. Soldán, P. & Hutson, J. M. Interaction of NH($X^3\Sigma^-$) molecules with rubidium atoms: Implications for sympathetic cooling and the formation of extremely polar molecules. *Phys. Rev. Lett.* **92**, 163202 (2004).
24. Hudson, E. R. Method for producing ultracold molecular ions. *Phys. Rev. A* **79**, 032712 (2009).
25. Wallis, A. O. G. & Hutson, J. M. Production of ultracold NH molecules by sympathetic cooling with Mg. *Phys. Rev. Lett.* **103**, 183201 (2009).
26. Wallis, A. O. G., Longdon, E. J. J., Żuchowski, P. S. & Hutson, J. M. The prospects of sympathetic cooling of NH molecules with Li atoms. *Eur. Phys. J. D* **65**, 151–160 (2011).
27. González-Martínez, M. L. & Hutson, J. M. Ultracold hydrogen atoms: A versatile coolant to produce ultracold molecules. *Phys. Rev. Lett.* **111**, 203004 (2013).
28. Rellergert, W. G. *et al.* Evidence for sympathetic vibrational cooling of translationally cold molecules. *Nature* **495**, 490 (2013).
29. Stoecklin, T. *et al.* Explanation of efficient quenching of molecular ion vibrational motion by ultracold atoms. *Nat. Commun.* **7**, 11234 (2016).
30. Li, M., Kłos, J., Petrov, A. & Kotochigova, S. Emulating optical cycling centers in polyatomic molecules. *Commun. Phys.* **2**, 1–10 (2019).
31. Domcke, W., Yarkony, D. & Köppel, H. *Conical Intersections: Electronic Structure, Dynamics & Spectroscopy* (World Scientific, Singapore, 2004).
32. Matsika, S. & Krause, P. Nonadiabatic events and conical intersections. *Ann. Rev. Phys. Chem.* **62**, 621–643 (2011).
33. Domcke, W. & Yarkony, D. R. Role of conical intersections in molecular spectroscopy and photoinduced chemical dynamics. *Annu. Rev. Phys. Chem.* **63**, 325–352 (2012).
34. Hoffman, B. C. & Yarkony, D. R. The role of conical intersections in the nonadiabatic quenching of OH($A\ ^2\Sigma^+$) by molecular hydrogen. *J. Chem. Phys.* **113**, 10091–10099 (2000).
35. Kendrick, B. K., Hazra, J. & Balakrishnan, N. The geometric phase controls ultracold chemistry. *Nat. Commun.* **6**, 7918 (2015).
36. Kendrick, B. K. Non-adiabatic quantum reactive scattering in hyperspherical coordinates. *J. Chem. Phys.* **148**, 044116 (2018).
37. Presunka, P. & Coxon, J. High-resolution laser spectroscopy of excited bending vibrations ($u2\leq2$) of the $\tilde{B}^2\Sigma^+$ and $\tilde{X}^2\Sigma^+$ electronic states of SrOH: Analysis of l-type doubling and l-type resonance. *Can. J. Chem.* **71**, 1689–1705 (1993).
38. Murad, E. Thermochemical properties of the gaseous alkaline earth monohydroxides. *J. Chem. Phys.* **75**, 4080–4085 (1981).
39. Werner, H.-J., Knowles, P. J., Knizia, G., Manby, F. R. & Schütz, M. Molpro: a general purpose quantum chemistry program package. *Comput. Mol. Sci.* **2**, 242–253 (2012).
40. Shao, Y. *et al.* Advances in molecular quantum chemistry contained in the Q-Chem 4 program package. *Mol. Phys.* **113**, 184–215 (2015).
41. Abrol, R. & Kuppermann, A. An optimal adiabatic-to-diabatic transformation of the $1^2A'$ and $2^2A'$ states of H$_3$. *J. Chem. Phys.* **116**, 1035–1062 (2002).
42. Maeda, K., Wall, M. L. & Carr, L. D. Hyperfine structure of the hydroxyl free radical (OH) in electric and magnetic fields. *New J. Phys.* **17**, 045014 (2015).
43. Petrov, A. N., Skripnikov, L. V., Titov, A. V. & Mawhorter, R. J. Centrifugal correction to hyperfine structure constants in the ground state of lead monofluoride. *Phys. Rev. A* **88**, 010501(R) (2013).
44. Baklanov, K. I., Petrov, A. N., Titov, A. V. & Kozlov, M. G. Progress toward the electron electric-dipole-moment search: Theoretical study of the PbF molecule. *Phys. Rev. A* **82**, 060501 (2010).
45. Alexander, M. H. Rotationally inelastic collisions between a diatomic molecule in a $^2\Sigma^+$ electronic state and a structureless target. *J. Chem. Phys.* **76**, 3637–3645 (1982).

Acknowledgements

Author contributions

S.K. supervised the project, M.L. and A.P. developed and coded the numerical methods for the scattering calculations. M.L, J.K., and H.L performed *ab initio* and scattering calculations, S.K. wrote first draft of the manuscript with contributions from M.L, J.K., and A.P.

Competing interests

The authors declare no competing interests.

Additional information

Correspondence and requests for materials should be addressed to S.K.

Reprints and permissions information is available at www.nature.com/reprints.

Publisher's note Springer Nature remains neutral with regard to jurisdictional claims in published maps and institutional affiliations.